CHEMISTRY OF
MATERIALS
Article

Chem. Mater. **2010,** *22,* 5543–5553 5543
DOI:10.1021/cm1015433

Short-Range and Long-Range Magnetic Ordering, in Third Generation Brannerite Type Inorganic−Organic Vanadates: $[\{Mn(Bpy)\}(VO_3)_2]\approx(H_2O)_{1.16}$ and $[\{Mn(Bpy)_{0.5}\}(VO_3)_2]\approx(H_2O)_{0.62}$

Roberto Fernández de Luis,[†] M. Karmele Urtiaga,[†] José L. Mesa,[‡] Karmele Vidal,[†]
Luis Lezama,[‡] Teófilo Rojo,[‡] and María I. Arriortua*[,†]

[†]*Departamento de Mineralogía y Petrología and* [‡]*Departamento de Química Inorgánica, Facultad de Ciencia y Tecnología, Universidad del País Vasco/EHU, Apdo. 644, E-48080 Bilbao, Spain*

Received June 3, 2010. Revised Manuscript Received July 28, 2010

The three-dimensional $[\{Mn(Bpy)\}(VO_3)_2]\approx(H_2O)_{1.16}$ and $[\{Mn(Bpy)_{0.5}\}(VO_3)_2]\approx(H_2O)_{0.62}$ inorganic−organic compounds, where Bpy is 4,4′-bipyridine, $(C_{10}H_8N_2)$, have been synthesized using mild hydrothermal conditions under autogenous pressure at 170 °C during three days, obtaining single-crystals suitable for X-ray structure determination. The compounds crystallize in the monoclinic system, space group $C2/m$, with a = 16.706(5), b = 3.5265(4), c = 11.558(5) Å, and β = 100.77(5)° for **1**, and a = 16.305(6), b = 3.5304(11), c = 17.788(6) Å, and β = 116.87(4)° for **2**. Single crystal X-ray diffraction reveals that both crystal structures are composed of inorganic layers pillared by organic ligands. However, **1** possesses simple layers, while **2** is constructed from double inorganic sheets. This structural organization gives rise to channels along the [010] direction, in which the crystallization water molecules are located. The thermogravimetry and thermodiffractometry experiments show that both crystal structures have a dynamical and reversible response to the removal and uptake of crystallization water molecules. Magnetic, ESR, specific heat, and neutron measurements indicate that both phases possess one-dimensional ferromagnetic coupling of the Mn(II) ions above the Néel temperature. Below 4 K for **1** and 7.5 K for **2**, a three-dimensional antiferromagnetic order is established. The sigmoidal shape of the magnetization curves indicates that the three-dimensional antiferromagnetic order can be reverted by the application of higher magnetic fields.

Introduction

The construction of new organic−inorganic hybrid compounds through the rational combination of organic ligands (“spacers”), metal nodes and different anions has become an area of great interest recently due to their potential application in catalysis,[1] hydrogen storage,[2,3] molecular adsorption,[4] electromagnetism,[5] and photochemistry,[6] among others. In the specific case of the vanadium oxides, recent interest has been focused on their potential use as secondary cathode materials for advanced lithium batteries[7] and their importance in the industrial oxidative catalysis and photocatalytic properties.[8]

From the point of view of hybrid vanadates with first row transition metal ions, the synthesis strategy is based on the synergetic interactions between the metal organic subnets and vanadium oxide subunits that give rise to several structural archetypes whose dimensionality can be partially controlled taking into account the different aspects of the structural organization.[9] The choice of bidentate ligands allows the possibility of obtaining extended metal−organic subnets and high dimensionality open crystal structures. In order to obtain extended hybrid frameworks, we choose Mn^{2+} due to the octahedral coordination preferences of this metal and bidentate ligands such as pyrazine, 4,4′-bipyridine or 1,2-di(4-pyridyl)ethene.[10,11] However, the modification of the hydrothermal synthesis conditions, such as time, temperature, stoichiometry, pH, concentration and filling factor, allows a partial control of the oxoanion polimerization degree giving rise to different $\{V_xO_y\}$ species stable in solution.[12]

---

*Corresponding author. Phone: 34-946012162. Fax: 34-946013500. E-mail: maribel.arriortua@ehu.es.

(1) Lee, J.; Farha, O. K.; Roberts, J.; Scheidt, K. A.; Nguyen, S. T.; Hupp, J. T. *Chem. Soc. Rev.* **2009**, *28*, 1450–1459.
(2) Rowsell, J. L.; Yaghi, O. M. *Angew. Chem., Int. Ed.* **2005**, *44*, 4670–4679.
(3) Fang, Q.-R.; Zhu, G.-S.; Ji, Y.-Y.; Ye, J.-W.; Xue, M.; Yang, H.; Wang, Y.; Qiu, S.-L. *Angew. Chem., Int. Ed.* **2007**, *46*, 6638–6642.
(4) Li, J.-R.; Kuppler, R. J.; Zhou, H.-C. *Chem. Soc. Rev.* **2009**, *38*, 1477–1504.
(5) Rao, C. N. R.; Cheetham, A. K.; Thirumurugan, A. *J. Phys.: Condens. Matter* **2008**, *20*, 083202.
(6) Férey, G. *Chem. Soc. Rev.* **2008**, *37*, 191–214.
(7) Chernova, N. A.; Roppolo, M.; Dillonb, A. C.; Whittingham, M. S. *J. Mater. Chem.* **2009**, *19*, 2526–2552.
(8) Lin, H.; Maggard, P. A. *Inorg. Chem.* **2008**, *47*, 8044–8052.
(9) Larrea, E. S.; Mesa, J. L.; Pizarro, J. L.; Rodriguez-Fernández, J.; Arriortua, M. I.; Rojo, T. *Eur. J. Inorg. Chem.* **2009**, *24*, 3607–3612.
(10) Hargman, J.; Hargman, D.; Zubieta, J. *Angew. Chem., Int. Ed.* **1999**, *38*, 2638–2803.
(11) Blatov, V. A.; Carlucci, L.; Ciani, G.; Proserpio, D. M. *CrystEngComm* **2004**, *6*, 378–395.
(12) Bouhedja, L.; Steunou, M.; Maquet, J.; Livaje, J. *J. Solid State Chem.* **2001**, *162*, 315–321.

Examples of those are the $\{V_2O_7\}$ dimers, $\{V_4O_{12}\}$ cyclic tetramers, or $\{VO_3\}$ metavanadate chains.[13] In that respect, we have recently reported the effect of the initial concentration and pH value in the hydrothermal synthesis of the Ni/Bpy/V_xO_y and Ni/Bpe/V_xO_y systems.[14]

From the point of view of magnetic properties, the vanadates constructed from short dipodal ligands such as $\{Cu_3(trz)_2\}(V_4O_{12})$[15] or $\{Co(pz)\}(VO_3)_2$[16,17] exhibit antiferromagnetic couplings through organic molecules. Recently, Maggard et al.[18,19] reported the low-dimensional magnetic and electrical properties of the reduced hybrid layered vanadate family $\{M(pz)\}(V_4O_{10})$ (M = Co, Ni, Zn), concluding that both ferromagnetic and antiferromagnetic spin correlations are present in all of the three materials, a condition which would lead to spin frustration. The increase of the ligand length gives rise to more open architectures such as $[\{Co_2(4,4'\text{-}Bpy)_3(H_2O)_2\}\text{-}V_4O_{12}]\ 2H_2O$ that exhibits a weak antiferromagnetic coupling of cobalt atoms at low temperatures or the $\{Co(4,4'\text{-}Bpy)\}(VO_3)_2$[20] and$\{Ni(Bpe)\}(VO_3)_2$[21] compounds showing a dimer isotropic antiferromagnetic behavior.

Surprisingly, the introduction of Mn^{2+} in the Bpy/V_xO_y system generates the $[Mn(Bpy)\}(VO_3)_2]{\approx}(H_2O)_{1.16}$ and $[\{Mn(Bpy)_{0.5}\}(VO_3)_2]{\approx}(H_2O)_{0.62}$ phases that possess edge shared manganese chains and the one-dimensional ferromagnetic ground state. The magnetic properties of both compounds are clearly related to the Brannerite type MnV_2O_6 inorganic vanadate, which consist of chains of edge shared MnO_6 octahedra parallel to the b axis and connected by chains of corner and edge shared VO_6 octahedra along the [100] and [001] direction. The magnetic behavior of the Brannerite type MV_2O_6 (M = Ni, Co and Mn)[22−24] family has been previously studied revealing very interesting features, such as the metamagnetism and 1/3 plateau magnetization in CoV_2O_6,[25] the disrupted antiferromagnetism in MnV_2O_6,[26] or the short-range and long-range magnetic ordering in the CuV_2O_6 phase.[27,28]

In this work, we describe the hydrothermal synthesis, crystal structures, thermal behavior, ESR measurements, magnetic properties, and specific heat of the third generation compounds $[\{Mn(Bpy)\}(VO_3)_2]{\approx}(H_2O)_{1.16}$ and $[\{Mn(Bpy)_{0.5}\}(VO_3)_2]{\approx}(H_2O)_{0.62}$ that combine the one-dimensional magnetism of the Brannerite type inorganic vanadates with the dynamical and reversible response to external stimuli, characteristic of some metal−organic frameworks.[29,30] Moreover, the magnetic structure of $[\{Mn(Bpy)\}(VO_3)_2]{\approx}(H_2O)_{1.16}$ has been determined by neutron diffraction measurements at low temperatures.

Experimental Section

Materials and Methods. Commercially available reagent grade chemicals were purchased from Sigma-Aldrich. These were used without further purification. All synthetic reactions were carried out in 50 mL Parr Teflon-lined acid digestion bombs. While only the best preparation methods leading to high purity and superior crystal quality for each of the reported compounds is described here, many reactions with varying reaction conditions (stoichiometry, reaction time, temperatures, pH value, and concentrations) were studied in the $MnCl_2\cdot 4H_2O/NaVO_3$/4,4′-bipyridine system. The main results are discussed in Supporting Information (Figure S1 and Figure S2). For **1**, a mixture consisting of $NaVO_3$ (0.76 mmol), 4,4′-bipyridine (2.27 mmol), $MnCl_2\cdot 4H_2O$ (2.27 mmol), and H_2O (40 mL) in the molar ratio 1:3:3 was placed in a 50 mL Parr Teflon-lined autoclave. The initial pH value was adjusted to 6.0 with a 1 M HNO_3 solution. After the mixture was stirred for 1 min, the autoclave was sealed and heated for 3 days in an electric furnace maintained at 170 °C. After the reaction, an orange microcrystalline phase together with a small amount of plate-like crystals of the same color is obtained. In the same preparation, a significant amount of unreacted Bpy was observed. In order to eliminate the excess of Bpy organic ligand, the samples were dispersed in ∼30 mL of ethanol and sonicated for 10 min. The water was poured off after allowing the polycrystalline sample to settle. This process was repeated until a pure sample of **1** was obtained, as judged by PXRD and visually under a microscope. The preparation of **2** was similar to that of **1** except the pH was adjusted to 4.0 with 1 M HNO_3 solution.

The patterns were recorded on a Bruker Advance Vårio diffractometer ($CuK\alpha 1$ radiation) for **1** (2θ range = 5−70°, step size = 0.015°, and time exposure = 10s per step) and on a Philips X'Pert diffractometer ($CuK\alpha$ radiation) for **2** (2θ range = 4−70°, step size = 0.02°, and time exposure = 15s per step). The Rietveld refinement, with a fixed structural model obtained from the single crystal X-ray diffraction, was carried out. For **1**, the refinement shows the existence of an extra maxima at 2θ = 28.2° related to the existence of a minor proportion (≈ 1%) unidentified impurity ($\chi^2 = 2.84$, $R_B = 12.1$, $R_p = 26.4$, and $R_{exp} = 19.76$) (Figure S3a, Supporting Information). The Rietveld refinement for **2** gives rise to a very poor fit due to the strong preferred orientation of the {0 0 L}

---

(13) Larrea, E. S.; Mesa, J. L.; Pizarro, J. L.; Arriortua, M. I.; Rojo, T. *J. Solid State Chem.* **2007**, *180*, 1149–1157.
(14) Fernández de Luis, R.; Urtiaga, M. K.; Mesa, J. L.; Rojo, T.; Arriortua, M. I. *J. Alloys Compd.* **2008**, *480*, 54–56.
(15) Hargman, P. J.; Bridges, C.; Greedan, J. E.; Zubieta, J. *J. Chem. Soc., Dalton Trans.* **1999**, 2901–2903.
(16) Khan, M. I.; Yohannes, E.; Goluv, V. O.; O'Connor, C. J.; Doedens, R. J. *Chem. Mater.* **2007**, *19*, 4890–4895.
(17) Zheng, L.-M.; Wang, X.; Wang, Y.; Jacobson, A. J. *J. Mater. Chem.* **2001**, *11*, 1100–1105.
(18) Yan, B.; Luo, J.; Dube, P.; Safat, A. S.; Goedan, J. E.; Maggard, P. A. *Inorg. Chem.* **2006**, *45*, 5109–5118.
(19) Bangbo, Y.; Olnteas, M. M.; Maggard, P. A. *J. Am. Chem. Soc.* **2007**, *129*, 12646–12647.
(20) Khan, M. I.; Yohannes, E.; None, R. C.; Ayesh, S.; Golub, V. O.; O'Connor, C. J.; Doedens, R. *J. Chem. Mater.* **2004**, *16*, 5273–5279.
(21) Fernández de Luis, R.; Mesa, J. L.; Urtiaga, M. K.; Lezama, L.; Arriortua, M. I.; Rojo, T. *New J. Chem.* **2008**, *32*, 1582–1589.
(22) Belaïche, M.; Bakhache, M.; Drillon, M.; Derrory, A.; Vilminot, S. *Physica B* **2001**, *305*, 270–273.
(23) Nakua, A.; Yun, H.; Reimers, J. N.; Greedan, J. E.; Stager, C. V. J. *Solid State Chem.* **1991**, *91*, 105–112.
(24) Kobayashi, S.; Mitsuda, S.; Ishikawa, M.; Miyatani, K.; Kohn, K. *Phys. Rev. B* **1999**, *60*, 3331–3345.
(25) He, Z.; Yamaura, J.-I.; Ueda, Y.; Cheng, W. *J. Am. Chem. Soc.* **2009**, *131*, 7554–7555.
(26) Klimber, S. A.; Attfield, P. *Phys. Rev. B* **2007**, *75*, 064406.
(27) Vasilèv, A. N.; Ponomarenko, L. A.; Smirnov, A. I.; Antipov, E. V.; Velikodny, Y. A.; Isobe, M.; Ueda, Y. *Phys. Rev. B* **1999**, *60*, 3021–3023.
(28) Vasil'ev, A. N.; Ponomarenko, L. A.; Antipov, E. V.; Velikodny, Y. A.; Smirnov, A. I.; Isobe, M.; Ueda, Y. *Phys. B* **2000**, *284−288*, 1615–1616.
(29) Kitagawa, S.; Kitaura, R.; Noro, S.-I. *Angew. Chem., Int. Ed.* **2004**, *43*, 2334–2375.
(30) Chen, C. L.; Goford, A. M.; Smith, M. D.; Su, C. Y.; zur Loye, H. C. *Angew. Chem., Int. Ed.* **2005**, *44*, 6673–6677.

Table 1. Crystal Data and Structure Refinement for Compounds 1 and 2

compound	(**1**)	(**2**)
formula	Mn C10 N2 H8 O7.16 V2	Mn C5 N H4 O6.62 V2
Fw (g/mol)	428.20	340.83
crystal system	monoclinic	monoclinic
color	orange	red
space group, N^{er}	*C*2/*m*, 12	*C*2/*m*, 12
a (Å), *b* (Å), *c* (Å)	16.706(5), 3.5265(4), 11.558(5)	16.305(6), 3.5304(11), *c* = 17.788(6)
β (°)	100.77(5)	116.87(4)
Z, F (000), T (K)	2, 421.2, 293(2)	4, 660.0, 150(2)
μ(mm^{-1})	2.336	3.379
ρ_{calc}., ρ_{obs}. (gr/cm^3)	2.123, 2.11(1)	2.479, 2.45(1)
crystal size (mm)	0.10 × 0.05 × 0.006	0.08 × 0.03 × 0.01
radiation (λ (Å))	0.71073	0.71073
N^{er} of reflns,	798	1282
reflns. ($I > 2\sigma(I)$)	594	846
h,*k*,*l* inter	$-20 \geq h \geq 20, -4 \geq k \geq 4, -14 \geq l \geq 14$	$-21 \geq h \geq 21, -4 \geq k \geq 4, -23 \geq l \geq 21$
R(int), *R*(sigma)	0.000, 0.0952	0.0509, 0.0722
*R*1, *wR*2(obs) ($I > 2\sigma(I)$)	0.0511, 0.0921	0.0290, 0.0509
*R*1, *wR*2(all)	0.1175, 0.1290	0.0543, 0.0533
GooF S	0.840	0.824
BASF	0.864(1)/0.136(1)	
N^{er} of parameters/restrains	86, 3	112, 31
L. diff. peak (e.Å^{-3})	1.584	1.041
L. diff. hole (e.Å^{-3})	−0.706	−0.474

family maxima. In order to corroborate the purity of the sample, the pattern matching analysis was carried out for **2**. The final fit shows a very good agreement with the initial monoclinic cell (χ^2 = 3.56, R_B = 1.04, R_p = 10.1, and R_{exp} = 6.98) (Figure S3b, Supporting Information).

Temperature dependent neutron powder diffraction data for **1** were collected on Instrument D1B at the ILL (Grenoble). The patterns were recorded in the 2−100 K temperature range, under vacuum and over the 2θ angular range 6.18°−85.98° (Figure S4, Supporting Information). The Rietveld method was used to refine the crystal and magnetic structures using the FULLPROF[31] program suite.

The percentage of the elements was calculated by atomic absorption spectroscopy (AAS) and C, N, H elemental analysis. **1** Found: Mn, 12.71(2), V 23.52(2); C, 27.80(2); N, 6.41(2); H, 2.35(3). Required: Mn, 12.78; V, 23.70; C, 27.94; N, 6.52; H, 2.42. **2** Found: Mn, 16.11(2); V, 29.55(3); C, 17.50(1); N, 4.08(1); H, 1.52(3). Required: Mn, 16.06; V, 29.78; C, 17.56; N, 4.09; H, 1.54. The density was measured by the flotation method in a mixture of bromoform/chloroform with 2.11(1)g/cm^3 for **1** and 2.45(1)g/cm^3 for **2**. The infrared spectra were recorded on a Jasco FT/IR-6100 spectrometer with pressed KBr pellets (400−4000 cm^{-1}) (Figure S5, Supporting Information).

Crystal Structure Analyses. Plate-like single crystals of $[\{Mn(Bpy)\}(VO_3)_2]{\approx}(H_2O)_{1.16}$ **1** and $[\{Mn(Bpy)_{0.5}\}(VO_3)_2]{\approx}(H_2O)_{0.62}$ **2**, with dimensions given in Table 1, were selected under a polarizing microscope and mounted on a glass fiber. Single-crystal X-ray diffraction data were collected at 293(2) K **1** and 100(2) K **2** on an XCalibur2 automatic diffractometer (Mo Kα radiation). The Lorentz-polarization and absorption corrections were made with the diffractometer software, taking into account the size and shape of the crystals.

The crystal of **1** is twinned. The two components of the twin are related by a rotation of 180° rotation about [100] reciprocal lattice direction (twin law: 100.540, 0−10, 00−1). The analysis of the initial data shows that all the measured reflections are partially overlapped. Moreover, the overlap of the lowest 2θ reflections is practically complete.[32] After the refinement, the masses of the two components of the twin were found to have percentages of 86.4(1) and 13.6(1) %.

The structures were solved by direct methods (SIR-92).[33] The refinements were performed by full-matrix least-squares based on F^2, using the SHELX97 program.[34] The crystal structures of both compounds were solved in the monoclinic space group *C*2/*m*. The carbon atoms belonging to the organic ligand and the crystallization water molecules were located in the difference density map. Anisotropic thermal parameters were used for all atoms except for the crystallization water molecules and the hydrogen atoms belonging to the organic ligand, which were fixed geometrically and allowed to ride on their parent carbon atoms (C−H 0.93 Å (**1**) and C−H 0.95 Å (**2**) U_{iso}(H) = 1.2U_{eq}-(C) Å^2). The pyridyl rings of the organic ligand are disordered in two positions related by symmetry. The occupation factors of the two disordered positions were restrained by symmetry to a 0.5 value.[35] The occupancies of the oxygen atoms belonging to the water molecules located in the channels were calculated from the weight loss observed in the thermogravimetric analyses (**1**, Occ.(Ow1) = 0.125; Occ.(Ow2) = 0.165; **2**, Occ(Ow1) = 0.125; Occ(Ow2) = 0.185). The hydrogen atoms attached to the crystallization water molecules were not located. Details of crystal data, data measuring and reduction, structure solution, and refinement are reported in Table 1. Further details on the crystal structure investigation may be obtained from the CCDC by quoting the depository numbers 777125 for **1** and 777126 for **2**.

Physical Measurements. Thermal analyses were performed in an air atmosphere, up to 500 °C, with a heating rate of 5 °C min^{-1} on a DSC 2960 Simultaneous DSC-TGA TA instrument. The temperature-dependent PXRD in an air atmosphere were carried on a Bruker Advance Vantec diffractometer (Cu*K*α radiation), equipped with a variable-temperature stage (HTK-2000) with Pt sample holder. The reversible water absorption was confirmed by temperature-dependent PXRD experiments in an air atmosphere. Those were carried on a Bruker Advance

---

[31] Rodriguez-Carvajal, J. *Phys. B* **1993**, *192*, 55–69.
[32] Spek, A. L. PLATON, A Multipurpose Crystallographic Tool; Utrecht University: Utrecht, The Netherlands, 1998.
[33] Altomare, A.; Cascarano, G.; Giacovazzo, C.; Guagliardi, A. *J. Appl. Crystallogr.* **1993**, *26*, 343–350.
[34] Sheldrick, G. M. *SHELX97, Programs for Crystal Structure Analysis*; Institüt für Anorganische Chemie der Universität: Göttingen, Germany, 1998.
[35] Watkin, D. *Acta Crystallogr., Sect. A* **1994**, *50*, 411–437.

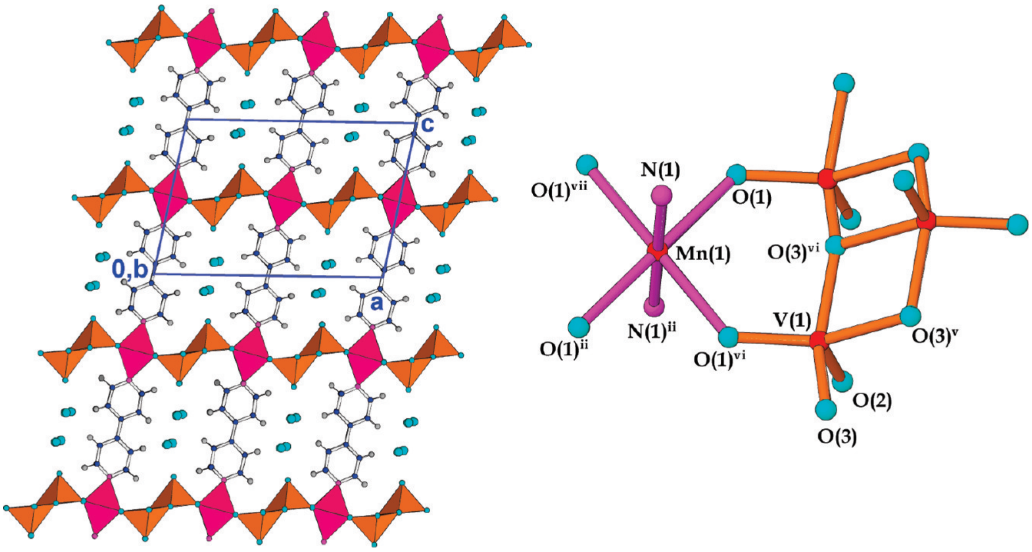

Figure 1. Crystal structure of compound **1**.

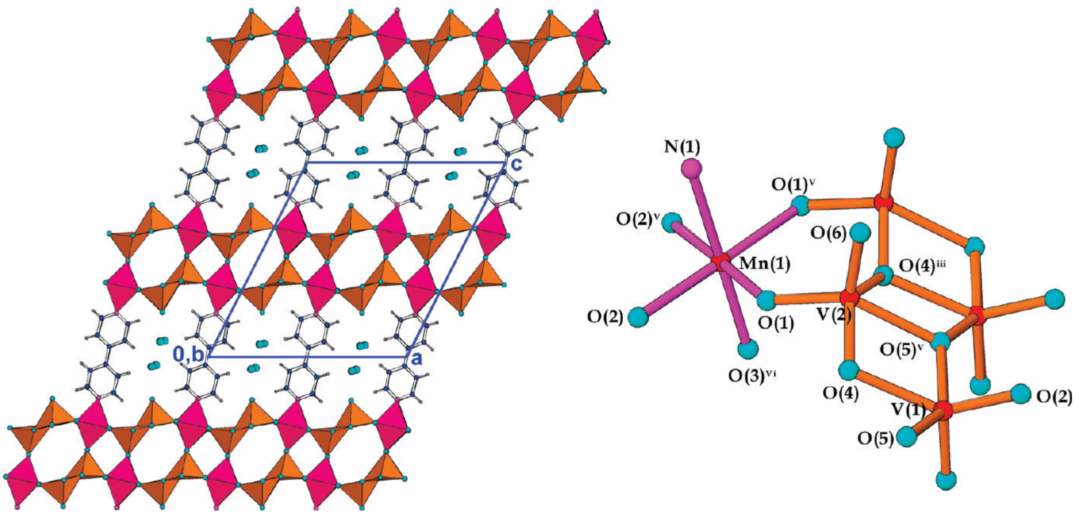

Figure 2. Crystal structure of compound **2**.

Vantec diffractometer (Kα radiation) equipped with a MRI TC-WIDE RANGE temperature chamber, which allowed us to obtain patterns down to −170 °C. A Bruker ESP 300 spectrometer was used to record the ESR polycrystalline spectra. The temperature was stabilized with an Oxford Instrument (ITC) regulator, the magnetic field was measured with a Bruker BNM 200 gaussmeter, and the frequency inside the cavity was determined using a Hewlett-Packard 5352B microwave frequency counter. The measurements were carried out at room temperature for both compounds and in the 300 to 4 K temperature range for **2**. Heat capacity measurements were carried out by a two-τ relaxation method, using a PPMS-system, with magnetic fields up to 9 T and temperatures down to 2 K. Magnetic measurements on the powdered sample were performed in the temperature range 2−300 K, using a Quantum Design MPMS-7 SQUID and CFMS (Cryogenic Ltd.) magnetometers. The measurements were carried out at 0.1, 0.25, and 0.5 T for **1** and 0.1, 0.5, and 5 T for **2**.

Results and Discussion

Crystal Structures. The title phases, $[\{Mn(Bpy)\}(VO_3)_2]{\approx}(H_2O)_{1.16}$ **1** and $[\{Mn(Bpy)_{0.5}\}(VO_3)_2]{\approx}(H_2O)_{0.62}$ **2** possess three-dimensional crystal structures that consist of inorganic $Mn(VO_3)_2$ layers pillared by the Bpy ligand. Compound **1** is constructed from simple inorganic layers, while **2** has double inorganic sheets between the organic pillars (Figures 1 and 2). Curiously, both crystal structures are formed from the same structural subunits: (i) edge shared manganese octahedra chains, (ii) edge shared VO_5 polyhedral zigzag chains, and (iii) the organic ligand.

For **1**, the coordination environment of the Mn atoms consists of four oxygen and two nitrogen atoms. The oxygen atoms of the octahedral equatorial plane are shared with two manganese atoms giving rise to edge shared octahedra chains along the [010] direction. The vanadium atom is five coordinated. The VO_5 polyhedra are edge shared giving rise to zigzag metavanadate chains. The MnN_2O_4 edge shared chains are corner linked to the vanadium atoms belonging to the metavanadate chains generating the inorganic layers of vanadate and MnN_2O_4 alternating chains (see Figure S6, Supporting Information). The layers are pillared by the organic Bpy ligand.

The vanadate chains of **2** are constructed from two crystallographically independent vanadium atoms, and the coordination environment of the manganese atoms consist of four oxygen atoms in the equatorial plane and one oxygen and nitrogen atoms in the axis of the octahedron. This one is slightly compressed in one of the axial directions, with a short Mn(1)−O(3)^{iv} (iv = $-x + 1/2, -y - 1/2, -z$) bond of 2.103(3) Å. The double layers of **2** can be described as the connection of two simple layers. This way, the manganese atoms of one of the simple layers are corner linked via the O(3) atom to the vanadate chains of the adjacent inorganic simple sheet (see Figure S7, Supporting Information). This connectivity generates six polyhedral intralayer channels. The double layers are pillared by the organic ligand that is directly coordinated to the manganese atoms (Figure 2).

For both compounds, the pyridyl rings of the Bpy ligand are disordered in two positions related by a mirror plane and hence are slightly rotated with respect to the (a,c) plane. The β angle (**1**, 100.77 (5)° and **2**, 116.87 (4)°) defines the inclination of the organic ligand with respect to the inorganic sheets. The disposition of the inorganic layers and the organic ligands generates channels along the [010] direction, in which the disordered crystallization water molecules are located.

The channels in which the crystallization water molecules are localized are very similar in both structures and possess sections of 5.5 Å × 3.5 Å for **1** and 5.8 Å × 3.3 Å for **2**. Both the channel geometry and the micropore limiting radius (3.5 Å) make these materials very interesting for their use in gas separation. Moreover, the pyridyl rings possess some degree of freedom to rotate around the ligand axis and could limit or favor the adsorption of different kinds of molecules.

The structures of the title compounds can also be envisioned as nets. The simplification of both crystal structures was carried out considering the manganese atoms as the nodes and the Bpy and metavanadate chains as the linker of the net.[36] The net of **1** is a 8-c uninodal net with hex-like topology (point symbol $\{3^6.4^{18}.5^3.6\}$, (Figure S8a, Supporting Information). For **2**, the topological analysis gives rise to a 9-c uninodal net with nci-like topology (point symbol $\{3^9.4^{22}.5^5\}$, (Figure S8b, Supporting Information).

Physico-Chemical Properties. The thermal and magnetic properties of both compounds are closely related because of the structural similarities. For this reason, the physico- and chemical properties will be discussed in a parallel way, showing only the results for one of the compounds, while those for the other one are provided in Supporting Information.

Thermal Analyses. The TGA and DTA curves resulting from the thermogravimetric analysis of both compounds show two steps of weightloss. The results are given in Supporting Information (see Figures S9a and S9b). The first one, with a value of 5.2% for **1** and 3.2% for **2**, corresponds to the loss of crystallization water molecules. The DTA curves of **1** and **2** suggest that the loss of crystallization water molecules occurs in two different steps (**1**, 20−40 °C, 2.1% and 40−70 °C, and 2.8%, and **2**, 20−40 °C, 1.3% and 40−65 °C, and 1.9%). The second weightloss takes place at high temperatures (**1**, 325−400 °C, 36.0%; **2**, 350−460 °C, 22.0%) and corresponds to the exothermic loss of one 4,4′-Bpy molecule per formula for **1** (calc 36.7%) and a half 4,4′-Bpy molecule per formula for **2** (calc 23.4%).

The thermal stability and the reversibility of the removal and uptake of water molecules in **1** and **2** were also studied by time-resolved X-ray thermodiffractometry in an air atmosphere. Compounds **1** and **2** are thermally stable up to 375 and 420 °C, respectively. However, the crystallinity of the patterns decrease dramatically by 320 °C for **1** and 375 °C for **2**. After the exothermic loss of the organic molecule, the Brannerite-like inorganic $Mn(VO_3)_2$ vanadate crystallizes at high temperatures (**1**, 375−500 °C; **2**, 420−375 °C) (Figure S10a and b, Supporting Information).

In order to corroborate the reversible removal−uptake of water, one heating and cooling cycle thermodiffractometries were carried out near the temperature ranges in which the transformations of the compounds occur. Figure 3a and b shows two representative 2θ ranges of the recorded patterns for compounds **1** and **2**, respectively.

For both compounds, two important displacements and intensity changes of some reflections take place in the heating process (**1**, 28 and 40 °C; **2**, 26 and 42 °C). The transformations are completely reversible with a hysteresis loop of 6 °C for **1** and 4 °C for **2**. The removal of the water molecules takes places also under vacuum. In a parallel way, the anhydrous samples were placed in ethanol and acetone. The X-ray patterns do not show any changes; therefore, these molecules are not adsorbed by the crystal structures, probably because their kinetic radii (acetone, 4.60 Å; ethanol, 4.53 Å) are bigger than the 3.5 Å limiting radii of the channels.

The thermal evolution of the cell parameters was determined by Rietveld refinement. Figure 4 depicted the thermal evolution (Figure 4a−e) and the relative thermal expansion of the cell parameters (Figure 4f) for **2**. The same analysis for **1** is shown in Figure S11 (Supporting Information). The structural changes due to the removal of crystallization water molecules give rise to important reductions of the a parameter (**1**, $a_{(10)}$ = 16.715(3) → $\mathrm{a}_{(34)}$ = 16.443(3) → $a_{(70)}$ = 16.281(3) Å; **2**, $a_{(10)}$ = 16.387(4) → $a_{(34)}$ = 16.224(4) → $a_{(70)}$ = 16.111(4) Å) and β angle (**1**, $\beta_{(10)}$ = 100.95(3) → $\beta_{(34)}$ = 102.00(3) → $\beta_{(70)}$ = 103.24(3)°; **2**, $\beta_{(10)}$ = 116.33(2) → $\beta_{(34)}$ = 116.92(2) → $\beta_{(70)}$ = 117.62(2)°) for both compounds. For **2**, an appreciable change in the c parameter is also observed (**2**, $c_{(10)}$ = 17.703(3) → $a_{(34)}$ = 17.752(3) → $a_{(70)}$ = 17.809(3) Å).

The thermal evolution of the cell parameters allows a qualitative description of the structural changes. Thus, the loss of solvent gives rise to a tilting of the Bpy pillars between the inorganic layers and hence an increase of the β angle value. However, surprisingly, the mayor

---

(36) Blatov, A. V. IUCr CompComm. Newslett. **2006**, *7*, 4−7. http://www.topos.ssu.samara.ru

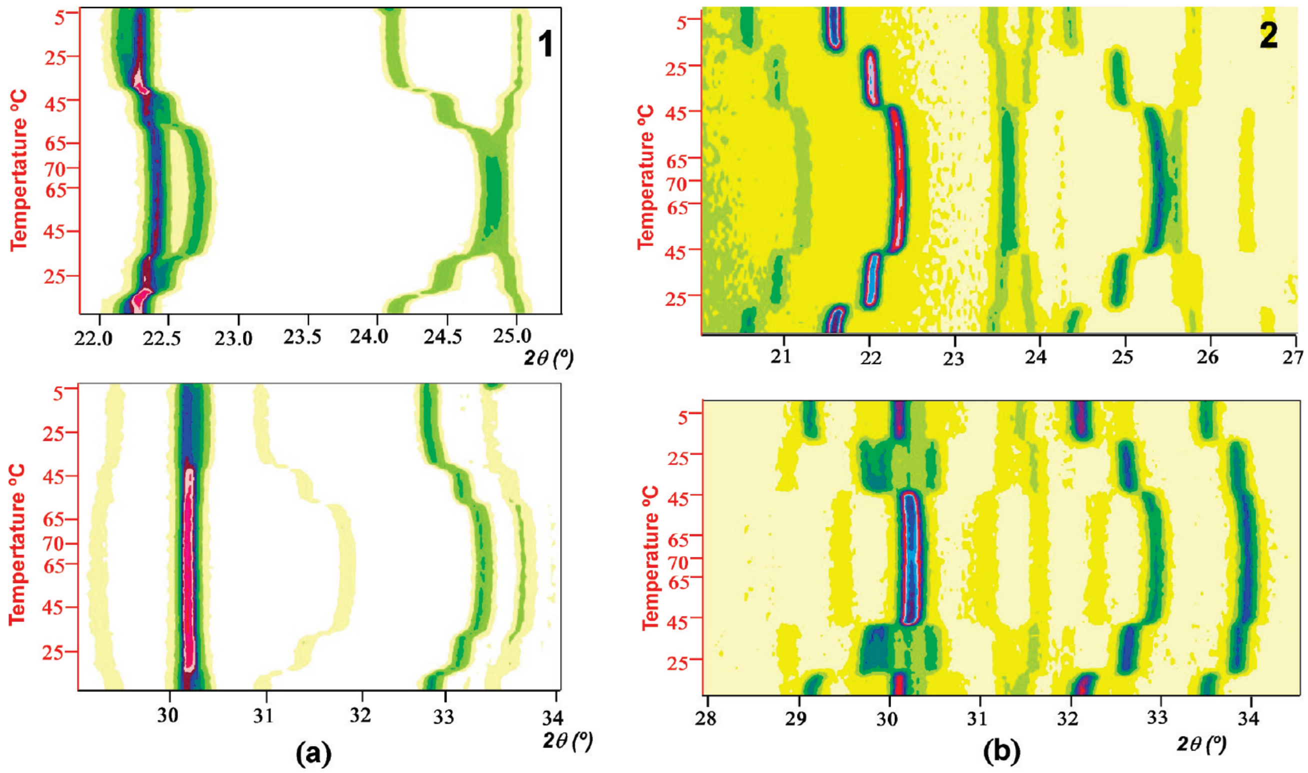

Figure 3. Thermal evolution of two representative 2θ (°) ranges for **1** (a: patterns were recorded every 2 °C, from 15° to 70 °C 2θ step = 0.03334°, 2θ range = 10−40°, time exposure = 1s). The same experiment was carried out on cooling between 70 and 5 °C for **2** (b: patterns were recorded every 2 °C, from 15 to 70 °C. The same conditions were used on cooling, from 70 to −10 °C).

structural changes are directly associated with the compression of the inorganic layers that generate the reduction of the *a* parameter. Qualitative models for the transformation pathways have been constructed (see Supporting Information, Figure S12). This way, the opposite tilt of the vanadate and manganese octahedra chains explains, qualitatively, the variation in the unit cell parameters for both compounds due to the removal of the solvent.

ESR Spectroscopy. The ESR spectra at room temperature were performed at X-band on powdered samples, and exhibit isotropic centered signals with line widths of 428G (**1**) and 354G (**2**). The values of g = 2.02(1) for (**1**) and 2.02(1) for (**2**) are slightly higher than that expected, 2.00, for a high spin Mn^{2+} ions in octahedral coordination.

The thermal variation of the ESR spectrum for **2** is shown in Figure 5. A continuous increase of the intensity between 300 and 30 K can be observed, in good agreement with a paramagnetic state of the manganese ions.

From 30 to 8 K, the ESR spectra show a decrease of the intensity and an increase of the line width and asymmetry, probably related to the short-range order ferromagnetic coupling between the manganese ions of the edge shared octahedra chains. The spectra registered at 8, 6, and 4 K are more asymmetric and intense than the other ones registered at higher temperatures. The intensity decrease and the line width and asymmetry increase between 8 and 4 K, suggest an antiferromagnetic ordering in this range of temperatures.

Magnetic Properties. The thermal evolution of the magnetic susceptibility was measured at 2−300 K with external fields of 0.1, 0.25, and 0.5 T for **1** and 0.1, 0.5, and 5 T for **2**. The results are shown in Figure 6 for **1** and Figure S13 (Supporting Information) for **2**. The χ_m and $\chi_m T$ curves registered at an applied field of 0.1 T show a continuous increase on cooling to maximum values of 5.23 cm^3/mol and 21.26 cm^3 K/mol at 4 K for **1** and 2.98 cm^3/mol and 21.50 cm^3 K/mol at 7.5 K for **2**. Below these temperatures, the χ_m and $\chi_m T$ curves decrease down to 2.40 cm^3/mol and 4.96 cm^3 K/mol at 2 K for **1** and 1.60 cm^3/mol and 3.13 cm^3 K/mol at 2 K for **2**.

Above 55 K (**1**) and 30 K (**2**), the inverse susceptibilities are fitted well by a Curie−Weiss law with Weiss temperatures of 16.9 K (**1**) and 16.3 K (**2**) and calculated Curie constants of 4.15 cm^3 K/mol (**1**) and 4.318 cm^3 K/mol. (**2**), in good agreement with the expected value for Mn^{2+} isolated cations (4.375 cm^3 K/mol). The $\chi_m T$ data were also fitted taking into account a homogeneous S = 5/2 chain in the 300−9 K (**1**) and 300−10 K (**2**) temperature ranges, applying the analytical expression for a regular chain derived from the Hamiltonian $H = -JS_i \cdot S_{i+1}$ (for local S = 5/2) (eq 1). The g values were taken from the ESR measurements. The best least-squares fitting parameters obtained are J = 1.142(4) K (**1**) and J = 1.516(7) K (**2**).[37] The most important constants obtained from the magnetic measurements are depicted in Table 2.

$$\chi_M = \left[\frac{Ng^2\mu_B S(S+1)}{3k_B T}\right]\left[\frac{1+u}{1-u}\right] \qquad (1)$$

---

(37) Carlin, R. L. *Magnetochemistry*; Springer-Verlag: Berlin, Germany, 1986.

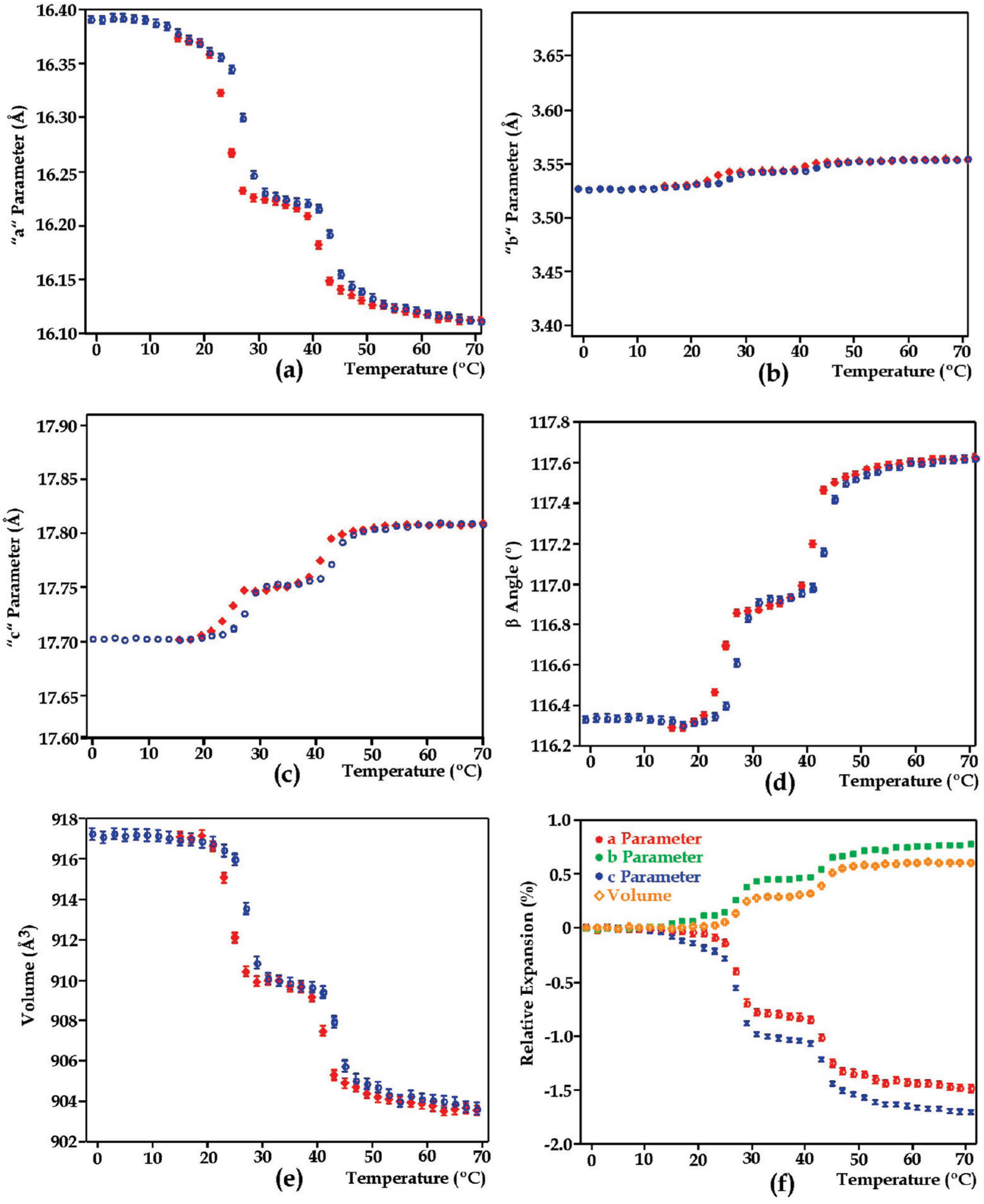

Figure 4. Thermal evolution of the cell parameters a−e and relative expansion of the cell parameters for compound **2**.

where

$$u = \coth\left[\frac{JS(S+1)}{k_BT}\right] - \left[\frac{k_BT}{JS(S+1)}\right] \qquad (2)$$

The positive values of Weiss temperatures and J exchange couplings indicate that significant ferromagnetic exchange interactions are present above the T_N. Probably, the ferromagnetic exchange takes place through the Mn−O−Mn bonds inside the chains of edge shared octahedra, giving rise to the increase of the χ_m and χ_mT curves between 300 K and Néel Temperatures. Below the maximum, (4 K for **1** and 7.5 K for **2**), a long-range three-dimensional antiferromagnetic order is established between the adjacent ferromagnetic chains giving rise to a sharp decrease in the χ_m and χ_mT curves.

The magnetization measurements performed above the T_N show a fast increase in the magnetization reaching values equivalent to five electrons for the Mn(II) ions

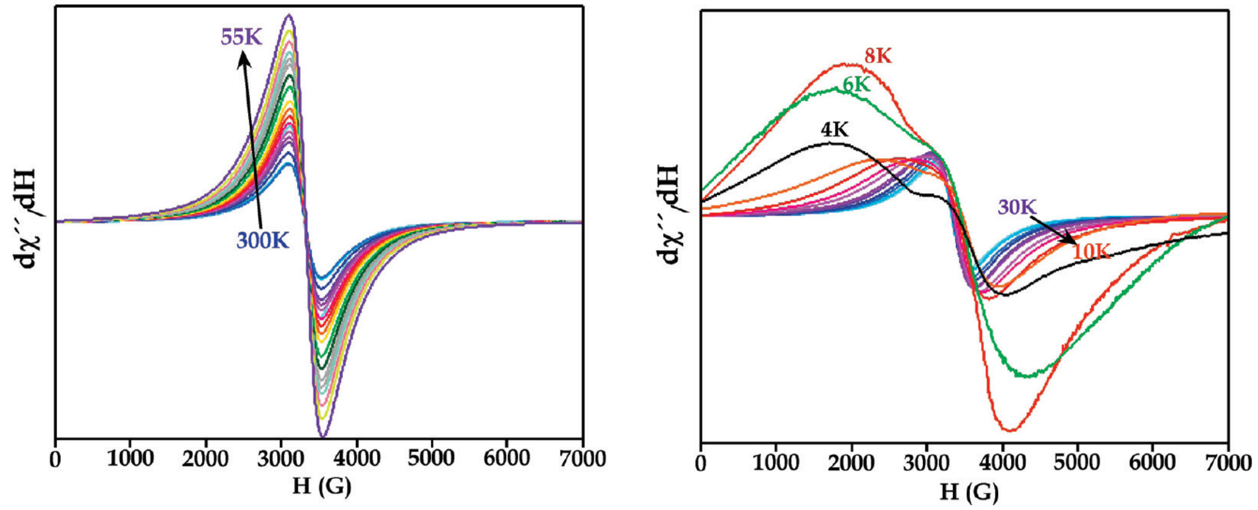

Figure 5. Thermal evolution of the ESR spectra in the 300 to 4 K temperature range.

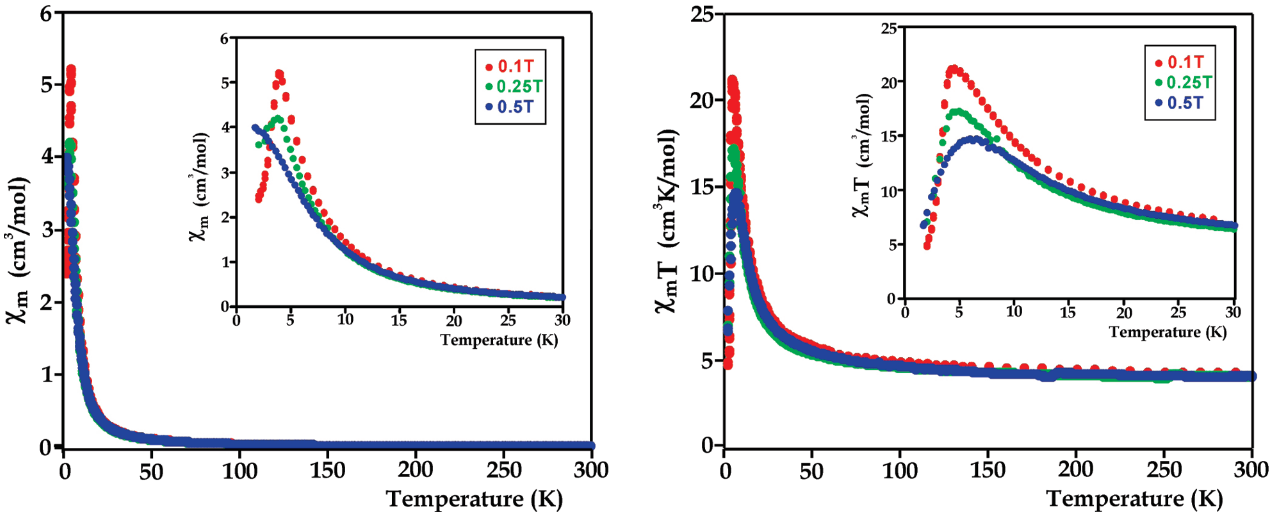

Figure 6. χ_m and χ_mT curves registered at 0.1, 0.25, and 0.5 T for compound **1**.

Table 2. Main Magnetic Data of Compounds 1 and 2

	Cm (cm^{3}K/mol)	θ (K)	Néel T (K)	J (K)	g
(**1**)	4.150	16.9	4	1.142(4)	2.02(1)
(**2**)	4.318	16.3	7.5	1.516(7)	2.02(1)

under moderate external fields (Figure 7 and Figure S14, Supporting Information). In both compounds, the dependence of the magnetization at 2 K shows a linear tendency below the expected values for a paramagnetic Mn(II) $S = 5/2$ cation at low applied fields, related to the long-range antiferromagnetic order. However, above a critical applied field (H_c = 0.2T for **1** and H_c = 0.4T for **2**), the magnetization curves for **1** and **2** show a fast increase lying above the $M/N\beta$ calculated values for an isolated $S = 5/2$ ion. No hysteresis was observed in either compound. The sigmoidal shape of the $M/N\beta$ vs H curves at 2 K indicates the field induced transitions from an antiferromagnetic long-range order to a one-dimensional ferromagnetic coupled system, which is characteristic of metamagnets.

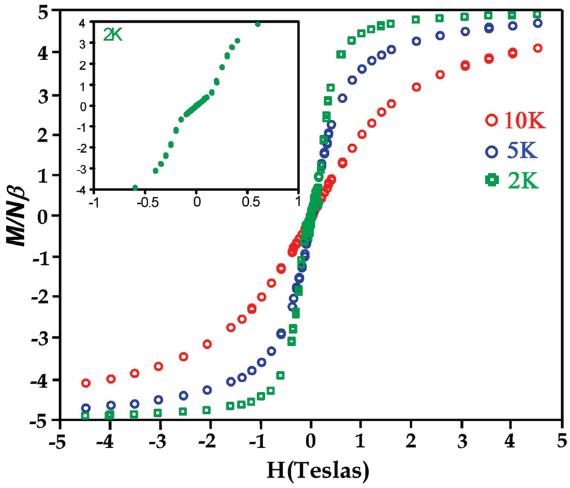

Figure 7. Magnetization measurements at 2, 5, and 10 K for compound **1**.

In order to characterize the metamagnetic behavior, field-cooled magnetization measurements were carried out under higher fields (Figure 6 and Figure S13, Supporting Information). At lower fields, the χ_m curves for **1** and **2**

Table 3. Debye Temperatures Obtained from the Crystal Lattice Contribution to the Specific Heat for 1 and 2

compound	θ_{D1} (K)	N_1	θ_{D2} (K)	N_2	θ_{D3} (K)	N_3
1	175.1	30.2	524.8	4.03	1944.6	6.66
2	202.9	20.9	657.1	3.8	2974	6.15

show a maximum at 4 and 8 K, clearly indicating the antiferromagnetic ordering. The magnetization maximum shifts toward low temperatures as the field is increased to 0.25 and 0.5 T for **1** and **2**, respectively. The χ_m curves at 0.5 for **1** and 5T for **2** show no maxima indicating that the interchain antiferromagnetic long-range ordering is overcome by the external field in both crystal structures.

Specific Heat. The field induced magnetic transitions have been confirmed by specific heat measurements. The C_p curves for **1** and **2** (Figure S15a and b, Supporting Information) show a λ-type anomaly at 3.5 and 7 K, respectively, indicating the establishment of a three-dimensional long-range antiferromagnetic ordering in both compounds. In order to estimate the lattice contribution (C_{pho}), the specific heat data were fitted to the Debye model, considering the existence of three different phonon spectra related to the different kinds of atoms present in the crystal structures (eq 1) (see Supporting Information Figure S15). The values for the Debye temperatures obtained from the best fits are depicted in Table 3.

$$C_{pho}(\theta_D) = 9R\left(\frac{T}{\theta_D}\right)^3 \int_0^{\theta_D/T} \frac{x^4 e^x dx}{(e^x - 1)^2} \qquad (3)$$

The magnetic contribution of C_p was calculated as $Cp_{mag} = C_p - C_{pho}$ for all of the magnetic applied fields. The C_{Mag} values for **1** and **2** are shown in Figure S16 (Supporting Information) and Figure 8, respectively. The Cp_{mag} curves possess a λ-type anomaly that indicates the existence of a three-dimensional ordering at low temperatures. Above the ordering temperature, a broader maximum is observed for both compounds but more clearly for **1**. The increase of the magnetic field generates the loss of the intensity and the progressive shift of the λ-type peak at lower temperatures, which is characteristic of antiferromagnetic interaction. The λ-type peak disappears at 10 KOe for both compounds. In a parallel way, the increase of the applied field generates the increase of the signal of the broader maximum located at higher temperatures than the λ-type peak. The existence of a broader peak suggests an important short-range ferromagnetic order. At higher applied fields, the three-dimensional long-range antiferromagnetic order is progressively overcome, and the one-dimensional coupling is favored. Hence, the λ-type peak, related to the three-dimensional antiferromagnetic order, lost intensity and is displaced progressively to lower temperatures, and the broader peak, related to the one-dimensional ferromagnetic coupling, increases its intensity.

The entropy was calculated at zero field and shows a continuous increase up to 35 K for both compounds, with entropy values of 14.4 J/Kmol (**1**) and 14.7 J/Kmol (**2**), very close to the expected one for one the Mn(II) ion (14.84 J/Kmol). At the ordering temperatures, the entropy values are 4.15 J/Kmol (**1**) and 6.18 J/Kmol (**2**), which correspond to the 29% (**1**) and 42% (**2**) of the maximum entropy for the systems. These results suggest that the effects of short-range ferromagnetic order above *Tc* are important. This fact is reflected in the low critical fields that are necessary to revert the antiferromagnetic long-range order to one-dimensional ferromagnetic coupled systems in **1** and **2** (Figure S17, Supporting Information).

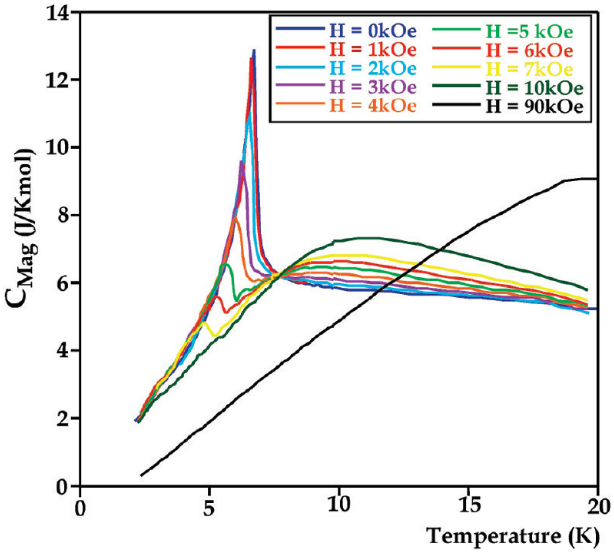

Figure 8. Applied field dependence of the C_{Mag} for compound **2**.

Neutron Diffraction. The D1B neutron diffraction patterns at 1.8 and 100 K for **1** are represented in Figure 9. Nuclear structure refinement at low temperatures showed that the $C2/m$ symmetry is maintained down to 1.8 K. The neutron diffraction experiments were carried out under vacuum conditions, and hence, the initial phase has been dehydrated. Also, the Ow1 and Ow2 occupation factors take near zero values after the refinement. However, we have to mention that the cell parameters are clearly close to those obtained from single X-ray diffraction for the hydrated compound. During the Rietveld refinement of the nuclear structure, the profile parameters, atomic positions (except the vanadium ones), and overall isotropic thermal parameter were adjusted. The patterns registered at 3 K and 1.8 K exhibit additional magnetic peaks, indicating that **1** is magnetically ordered at low temperatures. The magnetic peaks can only be indexed considering a magnetic lattice in which the unit-cell *c* parameter is duplicated with respect to the nuclear one, with a propagation vector of [1, 1, 1/2]. Consequently, the volume of the magnetic cell is two times larger than that of the nuclear unit-cell. Two intense reflections appear at $2\theta = 9.83$ and 11.79°. These (10−1/2) and (100) peaks arise from long-range antiferromagnetic order (see Figure 9).

The possible magnetic models were analyzed by performing a profile analysis of the patterns registered at 1.8 and 3 K by using the Rietveld method and including two phases: the nuclear contribution and a magnetic one. The magnetic peaks were fitted by an antiferromagnetic model, in which the Mn(II) ions on the (0, 0, 0) position are antiferromagnetically coupled to the Mn(II) ions in the (0, 0, 0.5) position and are aligned in the [010] direction. The fits for the patterns registered at 1.8 and 100 K are shown in Figure 9. Table 4 depicts the details of the Rietveld refinement of the patterns registered at 100, 30, 3, and 2 K.

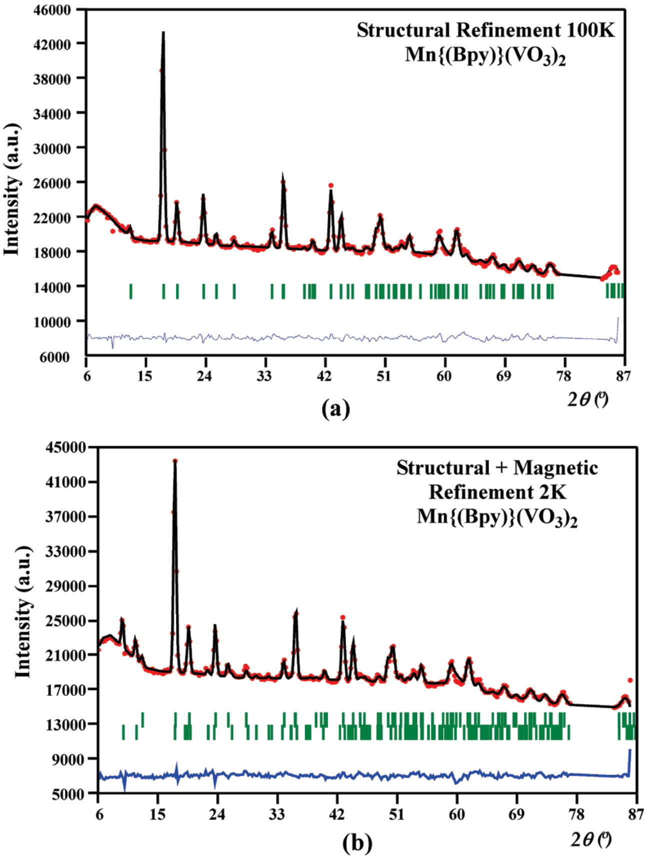

Figure 9. (a) Rietveld refinement of the structural model at 100 K. (b) Rietveld refinement of the structural and magnetic models at 2 K.

The best fit at 1.8 K ($R_{\mathrm{Mag}} = 27.1$) gives rise to a total moment aligned in the y direction of $M_y = M = 3.3(2)\mu_{\mathrm{B}}$. All attempts to refine the magnetic moments in the x and z directions give rise to values into the same order as its deviations; therefore, we opted for a model purely aligned in the y direction.

As the previously reported magnetic structure of $\mathrm{MnV_2O_6}$, the spin structure of **1** consists of ferromagnetic chains parallel to the y direction, with antiferromagnetic couplings to the nearest chains. This antiferromagnetic model can explain the double c parameter of the magnetic structure because the chains linked through the Bpy ligand in the [010] are antiferromagentically coupled, generating two independent Mn(II) ions in the magnetic structure (Figure 10).

The intensity of the magnetic reflections increases rapidly from 3 to 1.8 K. The magnetic moments obtained from the refinement of the patterns at 1.8 and 3 K show an important increase from 2.5(3) μ_{B} at 3 K to 3.3(2) μ_{B} at 1.8 K. However, the 3.3(2) μ_{B} value is far from the expected one of 5.92 μ_{B} for a Mn(II) $S = 5/2$ ion and still far from the 4.77(7) μ_{B} value reported for the $\mathrm{MnV_2O_6}$ Brannerite type compound.

As is reported previously, the studied phases are closely related to the Brannerite type inorganic vanadates, in which the vanadate groups are replaced by the Bpy organic ligand. In that respect, the increase of the shorter interchain distance from 4.964 Å in $\mathrm{MnV_2O_6}$ to 5.471 Å in **2** and 8.537 Å in **1** reduces the Néel temperature from 20 K in $\mathrm{MnV_2O_6}$ to 7.5 K and 4 K in **2** and **1**, respectively. Similar short-range ferromagnetic coupling above T_{N} and antiferromagnetic ordering below T_{N} are present in $\mathrm{CuV_2O_6}$ ($T_{\mathrm{N}} = 24$ K), $\mathrm{NiV_2O_6}$ ($T_{\mathrm{N}} = 20$ K), and $\mathrm{CoV_2O_6}$

Table 4. Thermal Evolution of the Magnetic Moment and Cell Parameters Obtained from Neutron Diffraction Experiments for Compound 1

		{Mn(Bpy)}(VO$_3$)$_2$		
temperature (K)	2 K	3 K	30 K	100 K
space group	$C2/m^a$	$C2/m^a$	$C2/m$	$C2/m$
a (Å)	16.726(3)	16.725(3)	16.731(3)	16.737(3)
b (Å)	3.5270(7)	3.5270(8)	3.5270(3)	3.5293(4)
c (Å)	11.587(5)	11.585(6)	11.584(2)	11.584(3)
β (°)	100.88(3)	100.89(3)	100.88(1)	100.86(1)
vol (Å^3)	671.2(4)	671.1(4)	671.3(2)	672.0(2)
instrument	D1B (ILL)	D1B (ILL)	D1B (ILL)	D1B (ILL)
radiation	2.525	2.525	2.525	2.525
monochromator	Ge(311)	Ge(311)	Ge(311)	Ge(311)
Z	4	4	4	4
2θ range (deg)	6−77, 83.5−86	6−77, 83.5−86	6−77, 83.5−86	6−77, 83.5−86
2θ step-scan increment (deg)	0.2	0.2	0.2	0.2
no. of reflections	136	136	136	136
no. of parameters	39	39	38	38
no. of restrains	17	17	17	17
reliability factors (%)				
R_p	21.5	21.8	19.7	23.0
Rw_p	13.4	13.6	12.5	13.5
R_{B}	8.75	9.02	7.88	9.50
R_{Mag}	27.1	34.2		
χ^2	1.66	1.22	2.78	3.18
mag. moment (μ_{B})	3.3(2)	2.5(3)		

[a] Symmetry of the nuclear structure $R_p = \Sigma|\gamma_{i,obs} - (1/c)\gamma_{i,calc}|/\Sigma\gamma_{i,obs}$, $Rw_p = [\Sigma w_i|\gamma_{i,obs} - (1/c)\gamma_{i,calc}|^2/\Sigma w_i[\gamma_{i,obs}]^2]^{1/2}$, $R_{\mathrm{B}} = [\Sigma|I_{obs} - I_{calc}|\Sigma I_{obs}]$.

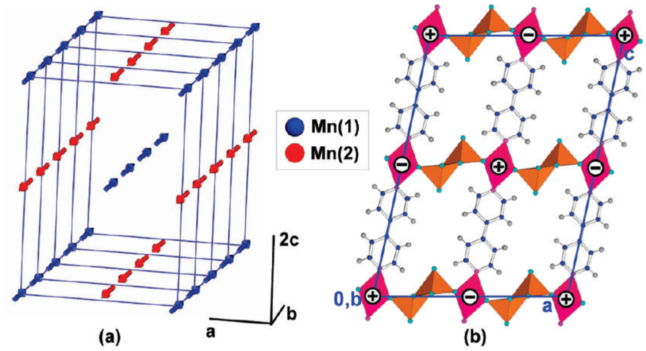

Figure 10. Magnetic structure for compound **1**.

(T_N = 7 K) compounds, but the latest one also exhibits a 1/3 magnetization plateau that may arise from the unusual competition between the interchain antiferromagnetic and ferromagnetic interactions. In a similar way, $YCa_3MnO_3(BO_3)_4$[38] also presents edge sharing manganese octahedra and exhibits a positive Weiss temperature of 27 K above T_N. In such chains, dominant antiferromagnetic direct exchange from e_g−e_g orbital interactions would be expected, but this may be outweighed by ferromagnetic t_{2g}−t_{2g} superexchange through the Mn−O−Mn bridges.

Conclusions

The structural characteristics of **1** and **2** are partially related to the synthesis conditions. The high vanadium concentration of the reaction media favors the existence of five coordination vanadium in both crystal structures. However, $[\{Mn(Bpy)\}(VO_3)_2]{\approx}(H_2O)_{1.16}$ is obtained at neutral or slightly acidic pH conditions containing simple inorganic layers and a more open crystal framework, while $[\{Mn(Bpy)_{0.5}\}(VO_3)_2]{\approx}(H_2O)_{0.62}$ crystallized at acidic pH conditions that generates double inorganic sheets and a more condensed architecture.

The title compounds possess open crystal structures, in which the solvent is located along the [010] channels between the inorganic layers and the organic ligand. The two thermal step release from the water molecules is clearly related to the existence of two crystallographically independent oxygen atoms in the [010] channels. In both crystal structures, the Ow(1) is located near the terminal oxygen atom belonging to the VO_5 polyhedra, suggesting the existence of a hydrogen bond. However, the distances of the Ow(2) with the host atoms are longer than those ones for the Ow(1), and hence, the possible interactions are weaker.

The temperatures at which the crystallization water molecules are evacuated from the crystal structure are very low, indicating the weak interaction between the solvent and the host. Despite these weak energies, the structures respond dynamically and reversibly to the crystallization water removal, and surprisingly, the major changes take place in the inorganic layers. Probably, the existence of weak points into the crystal structure allows this dynamic and reversible behavior characteristic of metal−organic frameworks. The radii of the channels limit the adsorbent of higher volume molecules than water, such as ethanol or acetone, into the crystal structure.

During the discussion of the magnetic properties, we have to taken into account that the crystal structures have a dynamical response to the loss of crystallization water molecules. As we have pointed out, the application of vacuum conditions give rise to the loss of water molecules in both compounds and hence to a dynamic response of the crystal structures. The magnetic and specific heat measurements are carried out under vacuum conditions, and more probably, the obtained results are related to the anhydrous compounds and not to the hydrated initial ones. We have discussed the magnetic properties as a function of the hydrated crystal structures; however, the major effect of the loss of crystallization water molecules is the reduction of the *a* parameter, which could affect the temperature of the antiferromagnetic long-range order.

The ESR, specific heat, and magnetic measurements confirm the antiferromagnetic ordering at low temperatures and also show the one-dimensional ferromagnetic coupling of the manganese atoms above the Néel temperature. Both compounds exhibit a field induced transition that occurs at low critical fields, overwhelming the weak antiferromagnetic ordering to a one-dimensional ferromagnetic coupling. The neutron diffraction experiments confirms the antiferromagnetic ordering below T_N; however, the patterns recorded above this temperature do not show any long-range ferromagnetic. The ESR, specific heat, and magnetic measurements indicate the existence of a ferromagnetic coupling above the Néel temperature. Thus, probably, this short-range ferromagnetic order is consistent with the observed parallel alignment of Mn(II) spins within the chains of edge shared Mn octahedra.

Acknowledgment. This work has been financially supported by the "Ministerio de Educación y Ciencia" (MAT2007-60400/66737-C02-01) and the "Gobierno Vasco" (IT-177-07 and IT-312-07), which we gratefully acknowledge. We thank the technicians of SGIker (UPV/EHU), Drs. J. Sangüesa, I. Orue, P. Vitoria, and A. Larrañaga, financed by the National Program for the Promotion of Human Resources within the National Plan of Scientific Research, Development and Innovation, "Ministerio de Ciencia y Tecnología" and "Fondo Social Europeo" (FSE), for the X-ray diffraction and magnetic measurements. R.F.d.L. thanks the MEC (Madrid, Spain) (BES-2005-10322) and Universidad del País Vasco/EHU for funding.

Supporting Information Available: Hydrothermal synthesis (PDF), IR spectroscopy (PDF), and crystallographic information files (CIF). This material is available free of charge via the Internet at http://pubs.acs.org.

---

(38) Li, R. K.; Greaves, C. *Phys. Rev. B* **2003**, *68*, 172403.